Materials & Design 220 (2022) 110796

Contents lists available at ScienceDirect

Materials & Design

journal homepage: www.elsevier.com/locate/matdes

Additively manufactured AlSi10Mg lattices – Potential and limits of modelling as-designed structures

Ulrike Gebhardt [a], Tobias Gustmann [b], Lars Giebeler [b], Franz Hirsch [a], Julia Kristin Hufenbach [b,c], Markus Kästner [a,d,*]

[a] Chair of Computational and Experimental Solid Mechanics, Institute of Solid Mechanics, TU Dresden, Dresden 01062, Germany
[b] Institute for Complex Materials, Leibniz Institute for Solid State and Materials Research Dresden, Dresden 01069, Germany
[c] Institute of Materials Science, Technische Universität Bergakademie Freiberg, Gustav-Zeuner-Str. 5, Freiberg 09599, Germany
[d] Dresden Center for Computational Materials Science (DCMS), Dresden, Germany

HIGHLIGHTS

- As-built and heat-treated AlSi10Mg specimen are used to parametrise a material model.
- Microstructural analyses explore the mechanical behaviour of bulk and lattices.
- Lattices are experimentally investigated in compression, tension, torsion and shear.
- The elastic–plastic material model predicts the mechanical behaviour of lattices.
- Powder, process parameters and geometry influence porosity and surface quality.

GRAPHICAL ABSTRACT

Additively manufactured AlSi10Mg lattices – Potential and limits of modelling as-designed structures

Ulrike Gebhardt,Tobias Gustmann,Lars Giebeler,Franz Hirsch,Julia Kristin Hufenbach,Markus Kästner

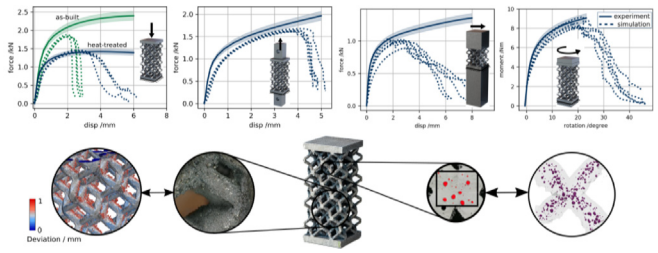

ARTICLE INFO

Article history:
Received 4 April 2022
Revised 25 May 2022
Accepted 26 May 2022
Available online 9 June 2022

Keywords:
Additive manufacturing
Lattice structures
Material characterisation
Al-based alloy
Elastic–plastic material model
Experimental characterisation

ABSTRACT

Additive manufacturing overcomes the restrictions of classical manufacturing methods and enables the production of near-net-shaped, complex geometries. In that context, lattice structures are of high interest due to their superior weight reduction potential. AlSi10Mg is a well-known alloy for additive manufacturing and well suited for such applications due to its high strength to material density ratio. It has been selected in this study for producing bulk material and complex geometries of a strut-based lattice type (rhombic dodecahedron). A detailed characterisation of as-built and heat-treated specimens has been conducted including microstructural analyses, identification of imperfections and rigorous mechanical testing under different load conditions. An isotropic elastic–plastic material model is deduced on the basis of tension test results of bulk material test specimens. Performed experiments under compression, shear, torsion and tension load are compared to their virtual equivalents. With the help of numerical modelling, the overall structural behaviour was simulated using the detailed lattice geometry and was successfully predicted by the presented numerical models. The discussion of the limits of this approach aims to evaluate the potential of the numerical assessment in the modelling of the properties for novel lightweight structures.

1. Introduction

The laser powder bed fusion (LPBF) process allows the near net-shape production of complex geometries such as lattice structures.

* Corresponding author at: Chair of Computational and Experimental Solid Mechanics, Institute of Solid Mechanics, TU Dresden, Dresden 01062, Germany.
E-mail address: markus.kaestner@tu-dresden.de (M. Kästner).

https://doi.org/10.1016/j.matdes.2022.110796
0264-1275/

Many studies have focused on lattices due to their high potential for tailored, lightweight, material-saving design types for a vast number of technological and biomedical applications [1–3]. However, there is an urgent need for reliable modelling approaches to predict the structural behaviour of the additively manufactured lattices [2,4]. Therefore, finite element analysis (FEA) is commonly used and such results are compared to the respective experiments.

The basis for building and characterising complex geometries such as lattice structures is to choose and understand the microstructure–property-relationship of a suitable alloy. The high demand for geometrically complex lightweight components drives the research and development activities on the processing of AlSi-based alloys for automotive and aerospace industry by additive manufacturing (AM) technologies, in particular LPBF. Especially Al12Si and AlSi10Mg, which are traditional Al casting alloys, are in focus of the investigations due to their widespread use, low material density, good mechanical properties, high corrosion and wear resistance [5–13]. Both alloys have a near-eutectic Si content and in consequence a small solidification range, which results in a good weldability and low susceptibility to cracking in the LPBF process [14]. If the applied powder material is spherical, e.g. characterised by the related good flowability [15], and properly stored at low moisture contents [16,17], a relative material density above 99% due to low amount of keyholes or gas pores can be easily achieved by using carefully selected process parameters that inhibit the occurrence of fusion defects [18].

The influence of the LPBF process on the microstructure and the mechanical properties of AlSi10Mg, also in comparison to the cast state, was already discussed [9,12,13,19]. The processing of high-strength aluminium alloys remains challenging due to their low laser absorption, high thermal conductivity and reduced powder flowability which results in high porosity ratios and increased cracking susceptibility [20,21]. By an appropriate LPBF-processing regime, a high tensile strength, elongation and hardness as well as good impact toughness can be realised [22]. This effect is traced back to the special, very fine microstructure that forms as a result of repeated fast melting in combination with a rapid cooling during the layerwise manufacturing [12]. To some extent, the AlSi10Mg alloy and its microstructural characteristics (grain size, texture and phase content) can be tuned by the process parameters to reach different cellular-dendritic structures, consisting of α-Al and a network of the eutectic Si phase [11]. This phase formation offers the possibility to adjust the material properties in situ and to combine the manufacturing of, for instance, complex parts with tailored local mechanical properties [23].

As discussed, there are many factors influencing the microstructural constituents and resulting properties of LPBF parts, like powder morphology, building direction, volume energy density or build-plate preheating [9,11,24]. Especially the heat treatment of the alloy is of great importance regarding damage tolerance and deformability. Conventional cast AlSi10Mg generally undergoes a heat treatment for obtaining improved mechanical properties, e.g. a T6 treatment implying solution treating, quenching and ageing [20,25]. By using LPBF, a beneficial fine-grained microstructure already exists in the as-built state. However, there are challenges like high residual stresses or varying properties in dependence of the building direction, which shall be reduced by an appropriate additional heat treatment. Thus, LPBF samples are often annealed at 300 °C to reduce residual stresses [12,26]. This approach, however, significantly alters the microstructure due to e. g. precipitation of new phases like Mg_2Si or changes in the element distribution and may significantly affect the deformation and fracture behaviour [25].

To numerically predict the mechanical behaviour of additively manufactured AlSi10Mg, different material models can be applied. Starting from linear-elastic [27] and elastic–plastic [28–30] up to models that include damage [31–33] or fatigue [34,35]. The decision for a certain material model is mostly a trade-off between complexity of the model, availability of material data, computational cost and accuracy of the prediction depending on the aim of the study. The applied models are usually parametrised through stress–strain data from bulk material tests [4]. Different models are applied in current literature to predict the structural behaviour of lattice structures. Based on the cell geometry and structural density of the structure the Gibson-Ashby model predicts effective material parameters [2,36]. The structural behaviour is evaluated using finite beam [27,37,38] or finite volume elements [31,38]. When modelling as-designed geometries of complex structures such as lattices, the transition between struts and nodes needs to be evaluated with respect to the stress distribution [39]. A suitable finite element type as well as the mesh sensitivity depending on the investigated parameters need to be taken into account [40].

The as-manufactured geometry can vary from the as-designed geometry due to geometric imperfections, that are inherent to the AM process. Those geometric imperfections present themselves as surface roughness [41], dimensional deviation [2], deviation of struts [27,42–45] and pores [29,31,46]. Their influence was shown by several studies through statistical representation [27,37] or the evaluation of as-manufactured structures [29,31,47–49]. Those geometric imperfections as well as material properties are dependent on the manufactured geometry and vary for example with the diameter and orientation of the struts of the lattices. A systematic evaluation of the development of material properties and imperfections through varying diameters of tension test specimens has been described by Dong et al. [23] and Sombatmai et al. [29].

To experimentally validate the numerical models on lattice structure specimens mostly compression tests are applied [2,27,31,38,50,51]. Other presented setups include tension [28,52], bending [50,51,53] or torsion [51] tests. The geometry of the lattice structure specimens and the design of their connectors to the testing machine vary with the corresponding experimental setup [3].

The scope of this study is to carefully deduce a feasible numerical model based on the experimental testing of additively manufactured AlSi10Mg bulk material specimens to predict the structural behaviour of lattice structure specimens in as-built as well as heat-treated states. However, extensive powder, part quality and microstructural analysis is mandatory. Generalised settings for the numerical models are evaluated and the chosen elastic–plastic material model can easily be parametrised with stress–strain data from tension tests on bulk material specimens to enable the applicability of the presented approach for larger and more complex structures. The structural behaviour is experimentally and numerically analysed and compared to the respective compression, shear, torsion and tension tests. The authors focus on the potential of this approach and how the mechanical behaviour of rhombic dodecahedron (RDC) lattice structures can efficiently be modelled using the as-designed geometry.

2. Materials and methods

2.1. Powder material and analysis

In the present study, a gas-atomised (argon) AlSi10Mg powder (EIGA technique: Electrode Induction-melting Gas Atomization) from Eckart TLS GmbH (formerly TLS Technik GmbH & Co. Spezialpulver KG), Germany, was applied. The chemical composition (see Table 1) of the powder material was determined using ICP-OES (Inductively Coupled Plasma Optical Emission Spectroscopy, iCAP 6500 Duo View, Thermo Fisher Scientific, USA)

Table 1
As-specified and experimentally determined chemical compositions of the powder material prior to processing (as-delivered, dried state). The nitrogen and carbon content with both < 10 ppm were below the detection limit of the applied method.

Specimen	Chemical composition/wt%									
	Al	Si	Mg	Fe	Cu	Zn	Ti	Mn	Ni	O
As-specified [54]	bal.	9 – 11	0.2 – 0.45	< 0.55	< 0.05	< 0.1	< 0.15	< 0.45	< 0.05	–
As-analysed	bal.	10.08 ± 0.05	0.5 ± 0.003	0.13 ± 0.001	< 0.005	< 0.002	< 0.006	< 0.005	< 0.005	0.092 ± 0.002

and was well within the range of the datasheet except for the slightly enhanced Mg content. The nitrogen and oxygen content of the powder were additionally analysed (minimum of three measurements) by carrier gas hot extraction (CGHE) in argon atmosphere (ON-836 Analyzer, LECO, USA). The carbon content was also determined by CGHE using an EMIA 820 V device from Horiba. The results of the chemical analyses are given in Table 1.

In order to clarify if the powder properties are suitable for the processing of a bulk material or more complex structures, the size and the shape of the gas-atomised AlSi10Mg powder was characterised in a first step by dynamic picture analysis and the most important values are summarised in Table 2. Most particles have a size/width of around 20μm to 30 μm without apparent particle satellites on the surface. The measured high particle symmetry value of 0.9 supported this observation.

To check the powder for possible particles with pores, like hollow spheres, a few milligramme of the as-delivered material were investigated using an X-ray computed tomography device (Phoenix nanotom, General Electrics, USA). The resolution of the tomography scan was adjusted to 2 μm and the scan was performed using a copper filter (0.3 mm in thickness) for the reduction of artifacts. 720 projections were recorded in total for each reconstruction. The volume analysis was performed using VG-Studio max 2.2 (Volume Graphics, Germany) and only a negligible number of hollow spheres (less than 2%) has been found. Hence, the solid density of the powder is close to the reference value of AlSi10Mg (2.67 g cm^{-3}, cf. Table 2) as confirmed via pycnometry (Pycnomatic ATC EVO, Porotec, Germany) prior to LPBF processing.

To link the particle analysis with the flow behaviour, first trials in a Hall flow meter with a cone diameter of 6 mm were performed. No free flow of powder and, thus, no evidence on the applicability for LPBF could be observed [55]. Only via manual tapping for a time of about three minutes, the powder passed the aperture. The dynamic measurements with a rotating drum (GranuDrum machine, GranuTools, Belgium) at 2, 4, 6, 8, 10, 20 and 40 rpm confirmed these assumptions by showing an irregular flow of the powder (see Appendix A). However, first spreadability tests in a selected SLM machine revealed, that the powder was suitable for layer-by-layer processing (see subsection 2.2).

2.2. Sample fabrication

All LPBF specimens were manufactured under argon atmosphere in a SLM250HL machine (400 W fiber laser, SLM Solutions Group AG, Germany). The residual oxygen level was manually controlled and adjusted at 0.2 wt.% before processing. The applied layer thickness was set to 50 μm and the scanning vectors between two subsequent layers, usually applied for SLM250 devices, were rotated by 79° (stripe hatching). In addition, the point distance and exposure time regarding the scan vectors were held constant at 1 μm and 1 μs, respectively.

Two sample sets of LPBF bulk material and lattice specimens (see Fig. 1) were produced using the standard build envelope of the SLM machine (248 × 248 mm^2) in combination with a feeder recoater. To obtain a satisfying powder layer homogeneity at high part quality, the aforementioned findings (powder analysis) were considered. In order to improve the recoatability and suppress agglomeration, a recoater with double-sized notches (width = 6 mm) inside the feeders was used. This recoater choice allowed a better powder delivery. Additionally the recoater speed was halved in order to suppress the formation of agglomerates during the bidirectional movement.

The produced bulk material samples (laser power = 350 W, scanning speed = 930 mm s^{-1}, hatching distance = 0.19 mm) had a diameter of 8 mm and a minimum length of 60 mm to allow the machining of tension samples according to ISO 6892/ DIN 50125 (sample type A, see Fig. 2a). Some of the bulk samples, without applying machining but using a heat treatment step (see below), were used for the microstructural analysis.

The desired lattice structure was a RDC [56]. This unit cell type can be manufactured via LPBF without the need of adding supports and, thus, was of high interest for our study and the processing of various horizontally orientated test specimens. A cell size of 10 × 10 × 10 mm^3 was used and the strut diameter d and strut length l were set constant at $d = 1.37$mm and $l = 4.32$mm, respectively. With respect to the testing setup and to guarantee a clamping of the lattice structures, the RDC cells were centred between plates (compression) or solid bars (tension, shear, torsion, see Fig. 2b) and manufactured as a triple stack (three samples per stack, see Fig. 1b) with similar process parameters (laser power = 350 W, scanning speed = 800 mm s^{-1}, hatching distance = 0.19mm) as for the bulk geometries.

All specimens were sandblasted with glass beads (150 μm to 250 μm) after processing to remove residual powder particles from the sample surfaces. For several samples an additional heat treatment step under a constant argon flow at 300 °C for 45 min, followed by air cooling, was applied before separating the sample stacks via electric discharge machining (EDM).

2.3. Part and microstructural analysis

The density of the bulk material specimens was obtained by the Archimedean method using a balance (Sartorius MC210P). Relative densities (around 99.73%) were calculated from these values by

Table 2
Overview and comparison of the determined powder characteristics (particle diameter, morphology, flowability and solid density) with the particle size distribution (PSD) supplied by the powder material data sheet from TLS Technik. The particle diameter corresponds to the width of the particles. The anisotropy describes the width-to-length-ratio of the particles [41] and should be close to 1 (perfect sphere). The flowability results shown here were determined by using the Hall flow meter with a funnel spout of 6 mm in diameter.

Specimen	PSD/μm			Particle morphology		Flowability/s	Solid density
	d_{10}	d_{50}	d_{90}	Anisotropy	Symmetry	∅6mm	/g cm^{-3}
As-specified [54]	10	28	44			–	
As-analysed	14	27	44	0.824	0.905	> 150	2.67 ± 0.01

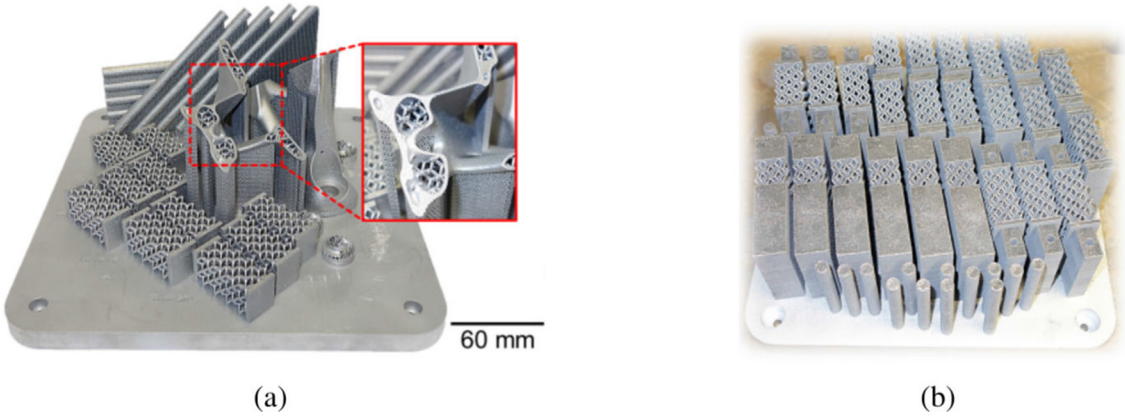

Fig. 1. Images of AlSi10Mg samples produced by LPBF. (a) Cylindrical samples, first compression test samples with an open cell structure (RDC) and geometrical prototypes, viz. impeller and reinforced hollow bracket (see inset). Please note that selected parts were already cut off the baseplate and are not shown here. The prototypes were not tested and just built to evaluate the suitability of the used process parameters for down- and up-scaled geometries. (b) Lattice specimens used for compression, tension, shear and torsion tests as well as further bulk tension samples.

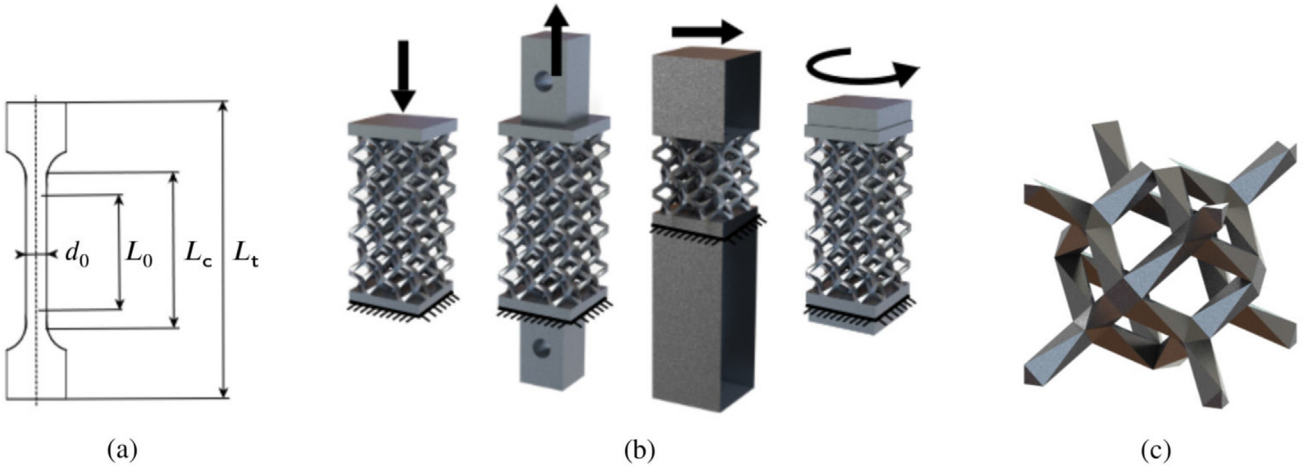

Fig. 2. Geometry of test specimens. (a) Material test specimen as defined in DIN ISO 6892: d_0 = 4 mm: diameter of cross section, L_0 = 25 mm: test length, L_c = 28 mm: parallel length, L_t = 60 mm: length of test specimen. (b) Lattice structure test specimens for compression, tension, shear and torsion experiments (from left to right). The cross section of the test specimens is 2 × 2 unit cells (20 mm × 20 mm). For the shear experiment the length of the test specimen is 2 unit cells (20 mm). The other test specimens have a length of four unit cells (40 mm). Loading conditions are visualised by black arrows. (c) Single unit cell with a structural density of 12.6%.

relating them to a density of 2.67 g cm^{-3} (AlSi10Mg, SLM Solutions material data sheet [54]).

The preparation of bulk material specimens was realised by polishing a small representative piece of 3 × 3 mm to about 80 μm in thickness. This sample was fixed to a polyacetate foil with an X-ray amorphous, quickly drying glue consisting of collodion in amyl acetate. X-ray diffraction measurements (mainly bulk, lattices: phase analysis via electron backscatter diffraction (EBSD), see below) were carried out on a STOE Stadi P diffractometer equipped with a Ge(111) primary beam monochromator and a Mythen 1 K position sensitive detector. Radiation of use was Mo $K_{\alpha 1}$ ($\lambda = 0.07293$nm). X-ray diffraction (XRD) data were analysed according to the Rietveld method [57] with the software package WinPlotR/ Fullprof [58]. As structure models, Si with the space group $Fd\bar{3}m$ [59], Al with the space group $Fm\bar{3}m$ [60] and Mg_2Si with the space group $Fm\bar{3}m$ [61] were used. Beside typical parameters, like (crystallographic) lattice parameters and phase contents, the microstructure parameter U of the Cagliotti equation was selected to compensate the isotropic line broadening originating from microstrain effects. To enable this parameter, the pseudo-Voigt function NPR = 7 was selected and an instrumental resolution function derived from a NIST 640d silicon standard analysis was deposited. No further analysis on the stress–strain behaviour was conducted as this part would lead beyond the scope of this report.

The microstructural characteristics of the bulk material and lattice samples were investigated by scanning electron microscopy (SEM) (Leo 1530 Gemini, ZEISS) in combination with energy-dispersive X-ray spectroscopy (EDX) and EBSD (XFlash4010, Bruker, Germany; e-FlashHR, Bruker, Germany). Therefore, the samples were firstly ground with P4000 SiC grit paper and subsequently fine-polished up to 0.25 μm with diamond suspension. For the SEM overview images and EDX analyses, the samples were furthermore etched with Keller's reagent. For the EBSD measurements, the specimens were not etched but further polished for 10 h using a VibroMet-2 Vibratory Polisher (Buehler, USA). A misorientation criterion of 15° was employed for the EBSD measurements. The minimum grain size of five pixels was chosen which is five times the value of the applied scan step of about 1 μm. Texture and grain size measurements were carried out using the software Esprit 2.3 (Bruker, Germany).

Furthermore, a selected lattice specimen (compression sample) was prepared for 2D pore analysis using the described preparation routine without etching. The area content of pores in selected

nodes of the lattice was determined using a confocal digital microscope (VHX–7000, Keyence) and the applied pore analysis module.

2.4. Mechanical characterisation

Test specimens of the bulk material with a cylindrical geometry according to Fig. 2a and building direction of 0°, 45° and 90° in the as-built and heat-treated state were used for tension testing. The experiments were performed at room temperature with quasi-static loading (Instron 5869, UK). The strain was measured with a laser extensometer (Fiedler Optoelektronik) and the applied strain rate was $5 \times 10^{-4} s^{-1}$. At least five samples were measured at each testing condition. To evaluate internal defects of the tested samples, selected specimens were analysed after the tension tests using a computed tomography scanner (FCT 160 IS, Finetec GmbH, Germany) with a resolution of 21 μm.

Heat-treated lattice specimens for compression, tension, shear and torsion loading were tested at room temperature (Zwick Roell 1475) with loading rates of 1 mm min^{-1} for the compression and tension, 0.39 mm min^{-1} for the shear and 6.3 °min^{-1} for the torsion tests. To evaluate the effect of the heat treatment on a structural scale, compression tests in the as-built state were performed as well. The tested geometries and test setups are schematically shown in Fig. 2b as well as the RDC unit cell geometry in Fig. 2c. At least three samples were used for each test setup. For the evaluation of internal defects, a compression test specimen was analysed by the Finetec GmbH micro-computed tomography (μCT) scanner with a resolution of 12 μm. Additionally the surface of a manufactured compression test specimen was investigated through optical microscopy (Keyence VK–X1050).

2.5. Modelling

An isotropic elastic–plastic material model with VON MISES yield surface and isotropic hardening is chosen to describe the material behaviour [62]. The linear elastic region is described by two constants: the POISSON ratio ν and the YOUNG modulus E. The YOUNG modulus is deduced from the experiments by evaluating the linear elastic region of the averaged stress–strain curves of the bulk material test specimens. To phenomenologically describe the isotropic hardening behaviour, the yield stress

$$\sigma_y(\overline{\epsilon}_p) = (1-\alpha)\cdot\sigma_{voce} + \alpha\cdot\sigma_{swift} \tag{1}$$

is modelled with an ansatz [63] using α as a weighting factor to combine the empirical hardening laws

$$\sigma_{swift} = A\cdot(\overline{\epsilon}_p + \epsilon_0)^n \tag{2}$$

by SWIFT [64] and

$$\sigma_{voce} = \sigma_{v0} + Q\cdot\left(1 - e^{-\beta\cdot\overline{\epsilon}_p}\right) \tag{3}$$

by VOCE [65]. Both hardening laws are well established to describe the high strain behaviour of metals and their combination yields the best results for this study. $\overline{\epsilon}_p$ is the equivalent plastic strain and the six parameters $A, \epsilon_0, n, \sigma_{v0}, Q$ and β are optimised to fit Eqs. 2 and 3 to experimental yield curves using the function lsqcurvefit from MATLAB R2017a. The VON MISES stress σ_v is applied in the yield criterion

$$f = \sigma_v - \sigma_y(\overline{\epsilon}_p) \leqslant 0. \tag{4}$$

Since there are two sets of bulk material test specimens – as-built and heat-treated – two sets of parameters are identified.

Virtual experiments on lattice specimens according to Fig. 2b are set up using the commercial finite element (FE) software ABAQUS CAE 2018. The geometric model is created via the PYTHON-API in ABAQUS CAE. The three translational degrees of freedom for the surface of the bottom plate are fixed and a reference point is kinematically coupled to the surface of the top plate for all four setups. The boundary conditions for the different setups are applied to the reference point. The structure's mechanical performance was evaluated by extracting the reaction forces at the reference point which were directly compared to the output of the experiments. The model was discretised with quadratic tetrahedral elements (C3D10).

Manufactured lattice structures will – due to the manufacturing process – always represent at least a small radius at the corners between two struts while as-designed geometries usually have sharp corners. Those sharp corners act as points of singularity in the numerical model which can lead to missing convergence of the FE mesh in the modelled structural behaviour. On the one hand a common solution for this discrepancy is the addition of artificial radii to take manufacturing induced shape deviations into account. On the other hand, including the radii in a unit cell geometry as shown in Fig. 2c can be difficult due to the many intersecting edges at the nodes. Additionally, very small radii require very fine meshes to resolve the geometry which will lead to high computational costs. Therefore, it is necessary to estimate the influence of the radii and the required level of detail to obtain a balanced cost-benefit ratio. To study the influence of different radii and sharp corners between struts on the effective numerical behaviour, a smaller node structure with varying technical radii as shown in Fig. 3a was evaluated.

To check the mesh quality of the numerical models, a relative error is introduced to take into account the change from one FE mesh to another. Rather than looking at the reaction force or present stress at one stage of deformation, the work W of the structure up to the displacement u_E where maximum force is reached in the corresponding experiment, is chosen as the significant quantity. Therefore, the relative error between two stages of mesh refinement is calculated by

$$\delta_i = \frac{|W_{i-1} - W_i|}{W_i} \qquad \text{with} \qquad W_i = \int_0^{u_E} F_i(u)\,du \tag{5}$$

where $F(u)$ is the evaluated reaction force over the displacement u up to the displacement u_E where the maximum force occurs in the experiment. The index i refers to the current mesh settings and $i-1$ to the next coarser mesh.

Compression tests are virtually performed on the node structure in Fig. 3a by fixing the vertical translational degrees of freedom at the bottom surface and applying a vertical displacement to the reference point whose translational degrees of freedom are constrained to the top surface of the structure using equation constraints. The length and width of the struts was chosen according to the lattice structures in Fig. 2b although the cross section is circular for easier application of the radii which are systematically varied within fractions of the strut diameter. The relative error as described in Eq. 5 is plotted for different numbers of elements in Fig. 3c. For the calculation, u_E is set to 0.3 mm and from one mesh setting to the next the number of elements is approximately doubled. For all radii the relative error falls below 2% as soon as the model consists of at least 30000 elements. For the biggest radius – $1/10^{th}$ of the strut diameter – the relative error is below 2% from the beginning and falls below 1% in subsequent refinement steps. In contrast, the relative error of the structure with no radius never reaches 1%. The mesh settings leading to about 30000 quadratic tetrahedral elements, where an initial seed size of 0.25 mm is applied, seem to yield sufficiently converged results even for the structures without radii while requiring reasonable computation time. Therefore, those settings will also be applied in the models of the lattice structures. WANG ET AL. [40] stated in their investigation

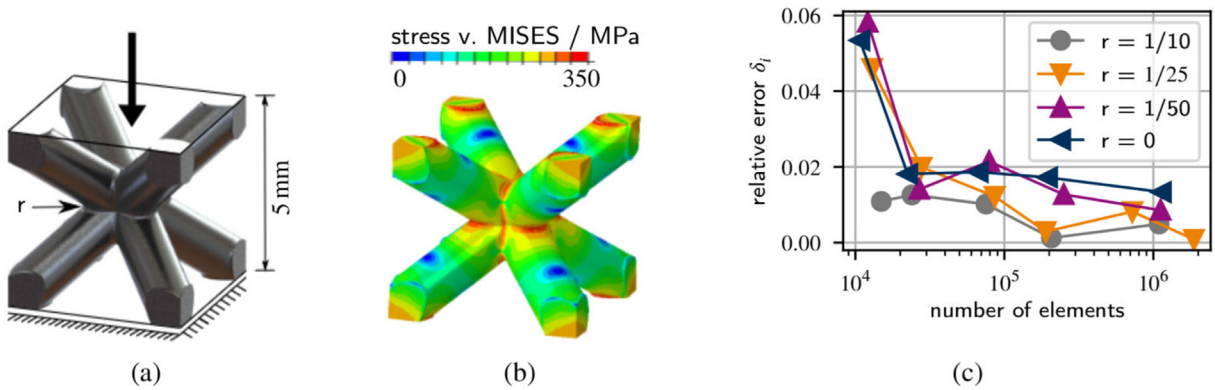

Fig. 3. Investigation of the structural behaviour of a representative node structure with varying technical radii r as a fraction of the diameter of the struts. (a) Geometry and boundary conditions of the model. (b) VON MISES stress for the structure with a radius of $1/50^{th}$ of the strut diameter. (c) Relative error of the results of virtual compression tests. The considered radii are given as fractions of the diameter of the struts.

of the convergence of homogenized elastic constants of lattice structures, that the radius of the lattice strut divided by the applied mesh size needs to equal $N_m = 8$ to acquire sufficiently converged results. The chosen mesh settings in this study lead to $N_m = 2.74$, keeping in mind that the investigated value is W, which is a much weaker requirement.

3. Results and Discussion

The focus of the present study is to model the structural behaviour of additively manufactured lattice structures in varying test setups on the basis of extensive material characterisation and subsequent validation. The bulk samples in the as-built and the heat-treated state as well as heat-treated lattices were characterised to be able to discuss the effect of the manufacturing process and properties on the structural behaviour.

3.1. Microstructure of the as-built and heat-treated alloy

The existing phases for the AlSi10Mg LPBF samples in the as-built and heat-treated states were analysed by XRD and the corresponding plots are given in Fig. 4a. The typical reflections for the Al and Si phase are indicated. The intensity of the Si reflections is rather weak due to a supersaturated Al matrix. This behaviour is also reported for other alloys like AlSi12 [7] and is attributed to the high cooling rates and the repetitive local remelting during LPBF [6].

To determine the contents of the phases in the as-built sample, a Rietveld analysis (2θ range: 10° to 60°) was performed (see Table 3). Thereby, a relative low content of 9 wt% of the Si phase in the as-built sample was observed in contrast to 14 wt% in the heat-treated samples. No clear reflections for the Mg_2Si phase were found in the XRD pattern. On the one hand, the Mg content with about 0.5 wt% (cf. Table 1) is above the upper nominal limit what might be positive for the precipitation of this phase [12]. On the other hand, the high cooling rates during LPBF might suppress the formation of this phase or it might stay below the detection limit.

In contrast to the as-built sample, the specimens after heat treatment at 300 °C showed slightly different phase contents. Beside the more pronounced reflections for the silicon phase (cf. Fig. 4a), the Rietveld analysis revealed the presence of the Mg_2Si phase (see Fig. 4b). The phase content was calculated to 0.5 wt%. Most studies have not reported on this effect or observed Mg_2Si precipitates, nor have they found a clear positive impact of Mg_2Si precipitates on the mechanical behaviour [66,67]. The main reason for this finding is the chemical composition of the atomised powder material that is closely related to the pre-alloy and the relative wide range of acceptable Mg contents.

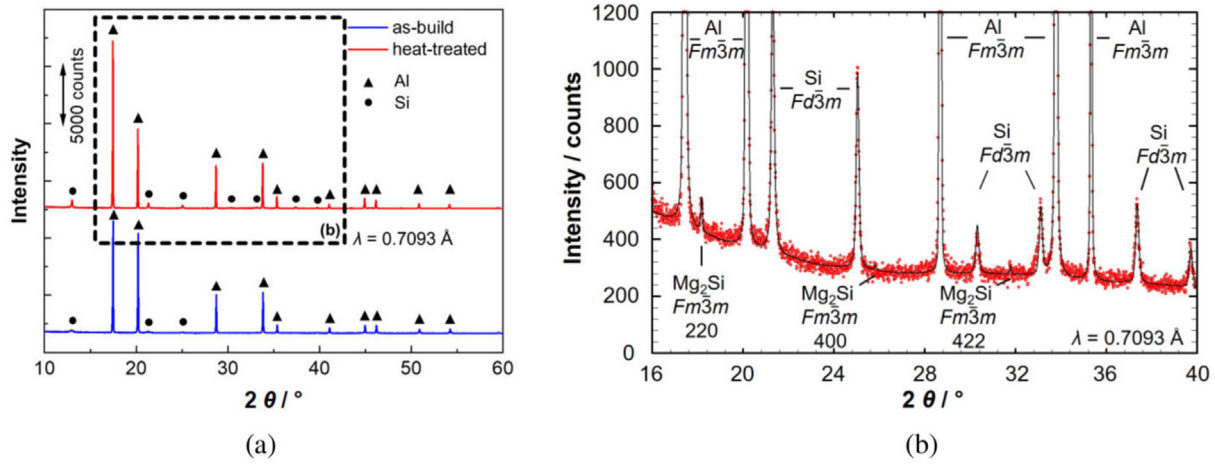

Fig. 4. XRD patterns of the AlSi10Mg bulk LPBF samples in the (blue) as-built and (red) heat-treated state. (a) The main reflections belong to the Al and Si phase. The magnified glancing angle range of the Rietveld analysis of the heat-treated sample (results are given in Table 3) is shown in (b) to differentiate between the main reflections and the impurity reflections of the Mg_2Si precipitate. This range is exemplarily inserted into the plot of (a) for better traceability.

Table 3
Phases and their structure from Rietveld analyses of the XRD patterns of the as-built and the heat-treated sample in Fig. 4.

Sample condition	Phase	Space group	Crystallographic lattice parameters		Phase content/wt%
			a/ Å	V/ Å^3	
As-built	Al	$Fm\bar{3}m$	4.0424(1)	66.059(3)	91
	Si	$Fd\bar{3}m$	5.426(3)	159.7(3)	9
Heat-treated	Al	$Fm\bar{3}m$	4.0424(1)	66.059(3)	86
	Si	$Fd\bar{3}m$	5.426(3)	159.7(3)	14
	Mg_2Si	$Fm\bar{3}m$	6.345(8)	256.4(9)	0.5

The LPBF process is typically known for the manufacturing of Al-based alloys with high cooling rates of a magnitude of about 105 K s^{-1} in average [68]. As a result of the rapid local solidification of the melted powder bed, the cross-section of as-built AlSi10Mg specimens shows a cellular microstructure consisting of a supersaturated Al phase (α matrix) and very fine Si segregations at the former melt pool and existing grain boundaries (see Fig. 5).

To better understand the influence of the heat treatment on the microstructure, SEM–EDX and SEM–EBSD analyses on the as-built (Fig. 5 (a) and (d)) and heat-treated bulk samples (Fig. 5 (b) and (e)) were performed and compared with the findings on the microstructure of the heat-treated lattice specimens (Fig. 5 (c) and (f)). It is important to note, that the lattice strut sizes are around 1.5 mm and that both specimen types were in good agreement with the indexed phase patterns (EBSD) and their grain sizes (bulk: average grain size = 13μm and median size = 6μm, lattice node point: average grain size = 10μm and median size = 3μm). The microstructure analysis for bulk parts (rods) were correlated with the obtained tension results (subsection 3.2). For the as-built state, the microstructures usually show an alignment of overlapping melt pools which has also been observed in this study via SEM and optical microscopy (not shown here). A slight difference in the melt pools was registered at higher magnifications regarding the grain formation in the centre (more elongated coarser grains, very fine cellular sub-grains around 1μm) and at the boarder or overlapping regions (more equiaxed smaller grains, coarser sub-structure) which is consistent with other findings [11,19]. The EDX mapping in Fig. 5 (d) displays a local segregation of Si along the grain boundaries. The Si mainly segregates as a network that wraps the Al matrix (see also [14]) but also Si precipitates in the Al grains (a few nanometres in size) are present. No clear enrichment of Mg was observed, what is also expected due to the very fine microstructure.

The change of the microstructure regarding the phases (distribution, morphology) and element concentrations (EDX mapping) due to the heat treatment is shown in Fig. 5 (e). The Si network decomposed and transformed into separated single particles (cf. Fig. 5 (d)). This observation was made for different heat-treated states where the annealing temperature ranged from 200 °C to 300 °C [19,67,69]. Due to the annealing, the local microstructure

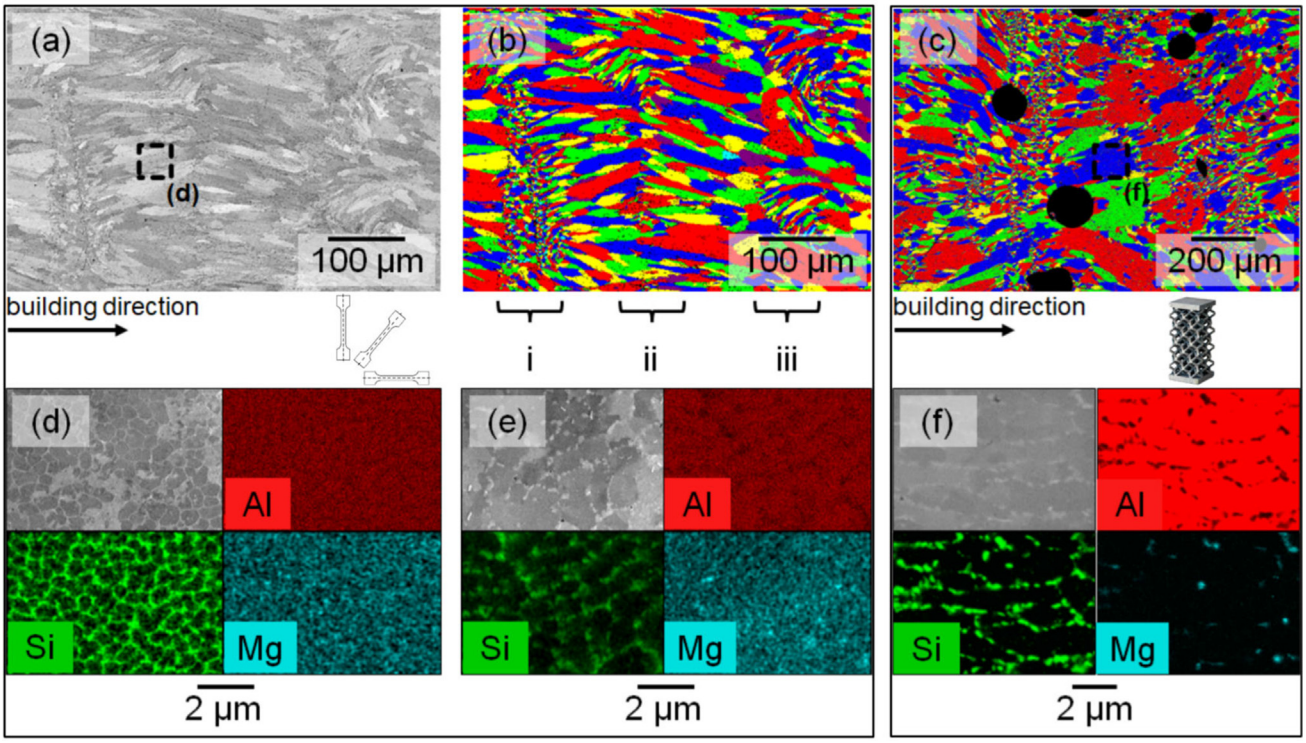

Fig. 5. Microstructure of AlSi10Mg LPBF bulk (as-built: (a), (b), (d) and heat-treated: (e)) and heat-treated lattice specimens (c) and (f) analysed via SEM. The images in (a), (b) and (c) show the grains ((a): SE-contrast) and corresponding EBSD maps (including zero solutions) of selected samples in building direction. The large black areas in (c) indicate pores. Three locations in the as-built bulk sample (b) are pointed out by the curly brackets showing the interfaces of at least two layers where clusters of smaller grains are formed due to the remelting by overlapping layers in these areas. The micrographs in (d), (e) and (f) show the SE-contrast images of the selected region for analysis and the corresponding EDX composition maps for the highlighted elements.

significantly coarsens (cf. SEM-images in Fig. 5 (d) and (e)). Basically, two groups of Si particles exist, namely elongated "coarser" ones (diameter: around 0.5 μm) and very small spherical particles (diameter: around 0.1 μm). While the coarser particles remain at the grain boundaries and originate from the former Si network, the smaller spheres are homogenously distributed and grew via a Si depletion of the former supersaturated matrix [70]. Interestingly, also segregations of Mg at several spots in the microstructure were found that were more visible than in the as-built states (cf. Fig. 5 (d) and (e)). This result corresponds well to the findings from XRD analyses and additionally confirms the presence of a small amount of Mg_2Si precipitates.

The Si network, identified by SEM analyses, is supposed to stiffen the material matrix. Its decomposition by a heat treatment step leads to a completely different mechanical behaviour (improved ductility) in comparison to the as-built counterparts (higher yield stresses and enhanced stresses at fracture) which will be further discussed in the following section and serve as a fundamental base for the mechanical behaviour of the heat-treated lattice specimens (subsection 3.3).

3.2. Mechanical behaviour of as-built and heat-treated bulk material specimens

The detailed analysis of bulk material parts and tension tests are the fundament for the characterisation of the material behaviour and subsequently the structural behaviour of lattice structures. Therefore, the results from the mechanical characterisation of bulk parts and the parametrisation of the material model are discussed in this chapter.

Exemplarily, four fractured bulk material specimens, each from one corner of the building platform, were analysed using CT scans. Fig. 6a schematically shows the position of the analysed part for each specimen and Fig. 6b – e visualise the identified pores within the specimens. Samples (b) and (c) are as-built test specimens while samples (d) and (e) underwent the heat treatment. An influence of the heat treatment on the identified pores of bulk material test specimens cannot be concluded from this investigation. Nevertheless, an increased porosity of the specimen in Fig. 6c is recognized. This sample was taken from the front left corner of the building platform and shows a much higher volume fraction of pores (0.15%) than the other samples (0.04% to 0.08%). Often, parts built on the left-hand side of the platform (laser scanning: left to right) can suffer from uneven layer thicknesses (energy input fluctuations and keyhole instabilities) due to process by-products like spatter (ejection of liquid particles from the melt pool, powder spatter [71]). As a relatively high number of bulk and lattice samples were manufactured per buildjob (high number of laser scanning paths), it seems likely that the transport of spatter by the gas flow (flow direction: left to right) during processing (samples in the centre and on the right-hand side) is one of the main reasons for the obtained density differences. Further effects like metal vaporisation (laser beam attenuation by plume formation [72]) can additionally trigger the local part quality but it is beyond the scope of the present study to fully clarify the aforementioned interrelations. It is noteworthy, that the described difference in residual porosity is not detrimental for the mechanical performance under quasi-static loading (see also subsection 3.3) [29] and was found within the range of other reports [73]. A comprehensive comparison is therefore possible.

Tension tests of the bulk material test specimens show a nonlinear material behaviour as plotted in Fig. 7a. The as-built specimens show an increased strength in contrast to their heat-treated counterparts (as predicted in subsection 3.1), e.g. endure higher yield stresses and show a more brittle fracture. Their yield stress as well as the plastic deformation behaviour is anisotropic (see insert in Fig. 7a). As mentioned, heat-treated samples have a lower yield stress, but show a much higher elongation at break which results in a more ductile fracture. As expected from the investigation of grain formation in subsection 3.1, the as-built specimens are characterised by a slight anisotropy as given in the insert in Fig. 7a where yield stress as well as the slope in the plastic deformation region varies with the building orientation. This anisotropy is much less pronounced than the effects of the heat treatment and will therefore be neglected in further discussions. The decrease in the yield strength, ultimate tensile strength and elastic modulus after heat treatment is explained with their respective microstructures described in subsection 3.1. The microstructural coarsening, detected by microscopic investigations, results in a reduction of the grain boundary area, which reduces the barrier effect for dislocation movement. Nevertheless, the formation of Si spheroids and Mg_2Si precipitates after the heat treatment results in a strengthening effect, but the grain size effect still dominates (increasing grain size, decreasing deformability, cf. Figs. 5 and 7a). Furthermore, the fracture of the as-built AlSi10Mg samples is promoted by the propagation of cracks through the brittle Si network along the boundaries of the Al phase.

Fig. 7b compares the results of this study with elongations A and ultimate tensile strengths R_m documented in the literature. For the orientation of 0° and 90°, the as-built specimens are in good agreement with the data sheet. For the heat-treated specimens, elongation agrees well with the data sheet while the tensile strength R_m is strongly decreased. Compared to this results and those from the data sheet [54], the presented as-built parameters

Fig. 6. Visualisation of macroscopic pores in fractured bulk material test specimens using Simpleware™software (ScanIP, Version 0–2018.12). (a) The circle schematically shows the analysed part of the fractured specimens. (b) – (e) Scanned pieces of the test specimens with a diameter of 4 mm. The samples (b) and (c) are as-built parts and the samples (d) and (e) underwent a heat treatment. The volume fraction of the identified pores is given for each specimen in the subcaption.

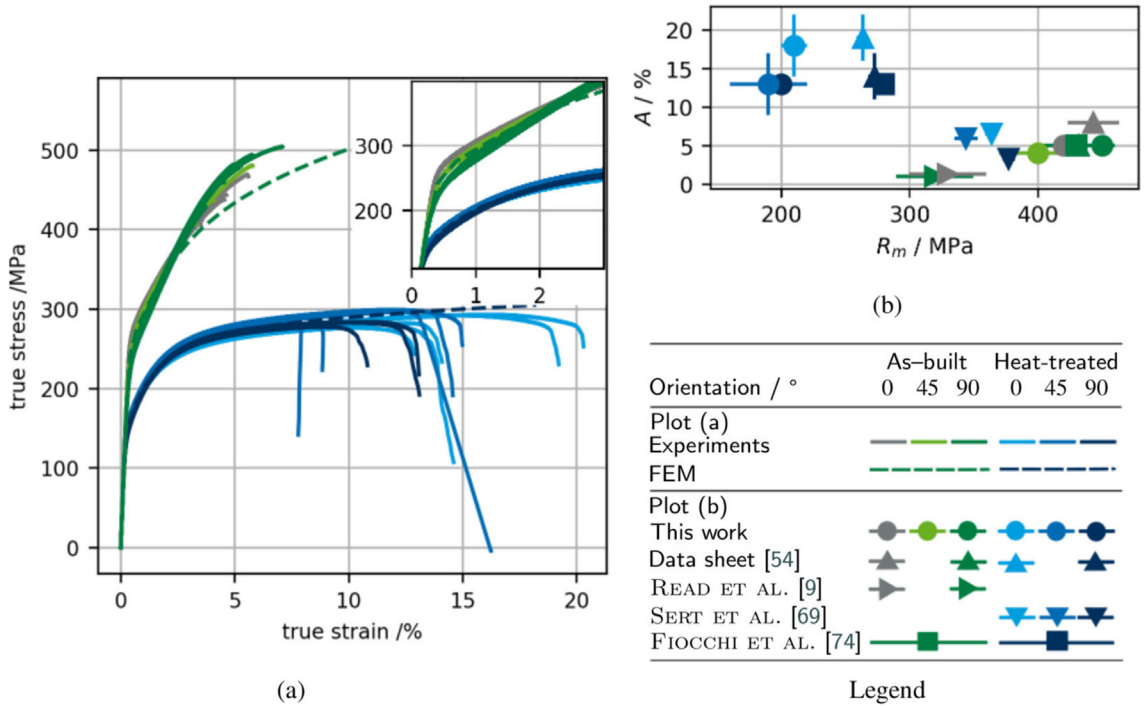

Fig. 7. Results from tension tests on bulk material test specimens. (a) Stress–strain curves and FEM results from one-element tests. (b) Elongation at break over ultimate tensile strength compared to results from literature.

in Fiocchi et al. [74] coincide with the values given here while the specimens from Read et al. [9] show lower elongation and tensile strength. Sert et al. [75] stated much higher tensile strength for lower elongation for heat-treated specimens and Fiocchi et al. [74] reports similar elongations but again much higher tensile strength compared to this study.

With the averaged results from those tension tests on bulk material test specimens, an isotropic elastic–plastic material model, as described in subsection 2.5, is parametrised for the as-built and the heat-treated test specimens respectively. The as-built model was fitted only up to 1% plastic strain and the heat-treated model up to 5% plastic strain to improve the model response especially in the small-strain range. For higher strain values the model extrapolates. The identified parameters are listed in Table 4. The poisson ratio is chosen to be $\nu = 0.35$ according to the extensive work of Sert et al. on additively manufactured AlSi10Mg [75]. The results from numerical tension tests on a single hexahedral element are shown as dashed lines in Fig. 7a. The modelling of the as-built material agrees with the corresponding experiments up to 2.5% strain while the model for the heat-treated material corresponds with its experiments almost up to 15% strain. Therefore, the elastic–plastic behaviour for an uniaxial tension is well captured by the material model.

3.3. Mechanical behaviour of lattice structures

The experimental results on lattice specimens are compared to their corresponding virtual experiments on as-designed lattice structures for four different load setups as introduced in subsection 2.5. The potential and limits of this modelling approach are evaluated in this section.

The as-designed geometry of lattice structures can already be very complex and the addition of radii in the sharp corners between struts is often complicated and not necessary for creating the input file for the manufacturing process. Those sharp corners represent numerical singularities in the virtual setup as discussed in subsection 2.5. To reinforce the findings from Figure 3, Figure 8 evaluates the relative error according to Eq. 5 for the virtual setups of the lattice structure test specimens. The as-designed geometry and the identified material parameters for heat-treated specimens as shown in Table 4 are applied for varying mesh sizes. Mesh settings comparable to the identified settings in Subsection 2.5 lead to 1.7 million elements for the compression test specimen. Looking at the circle markers in Fig. 8 depicting the more extensive evaluation of mesh sizes for the compression test setup, 1.7 million elements allow the relative error δ_i to drop to 2% as expected. This seed size is kept constant for tension, shear and torsion tests since the lattice geometry is the same for all setups. Their corresponding relative error is below 4% for shear and torsion test and about 2% for the tension test.

The results of the lattice structure experiments are compared to their virtual equivalents in Fig. 9. A good qualitative agreement between experiments and numerical results is reached for all four setups. The force–displacement behaviour is slightly overestimated by all models. The largest gap seems to appear between the experimental and numerical results of the tension tests. The relative error is still inherent within the numerical results, as discussed in the previous paragraph, and is accounted for by the

Table 4
Parameters for the material model for as-built and heat-treated parts as described in Eqs. (1)–(3).

	E/ MPa	ν	α	A	ϵ_0/ MPa	n	k_0/ MPa	Q	β
As-built	71931	0.35	1.9375	315.9012	0.0017	0.1186	191.456	124.6509	3.5885
Heat-treated	71638	0.35	0.4774	213.7848	0.0163	0.1729	134.3954	130.8835	0.9471

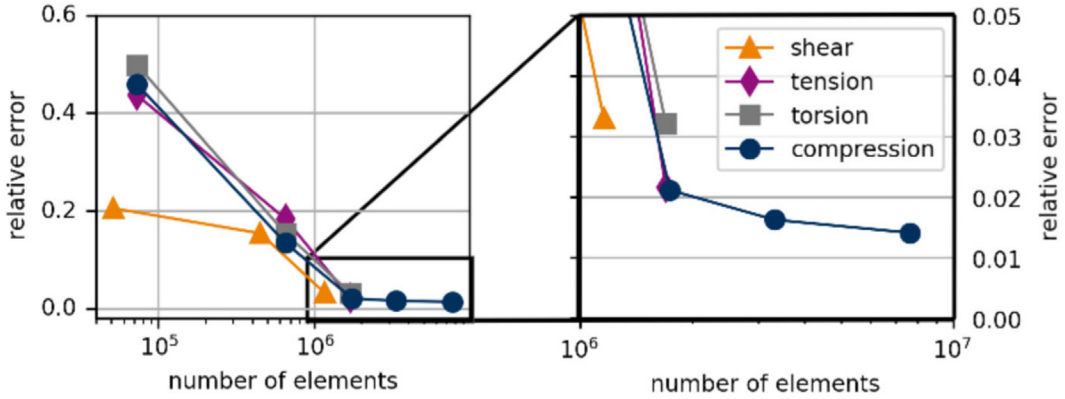

Fig. 8. Comparing deviation in work up to the point of maximum force in the experiments for all four setups, being 2.7 mm for the compression test, 2 mm for shear test, 4 mm for tension test and 20° for torsion test.

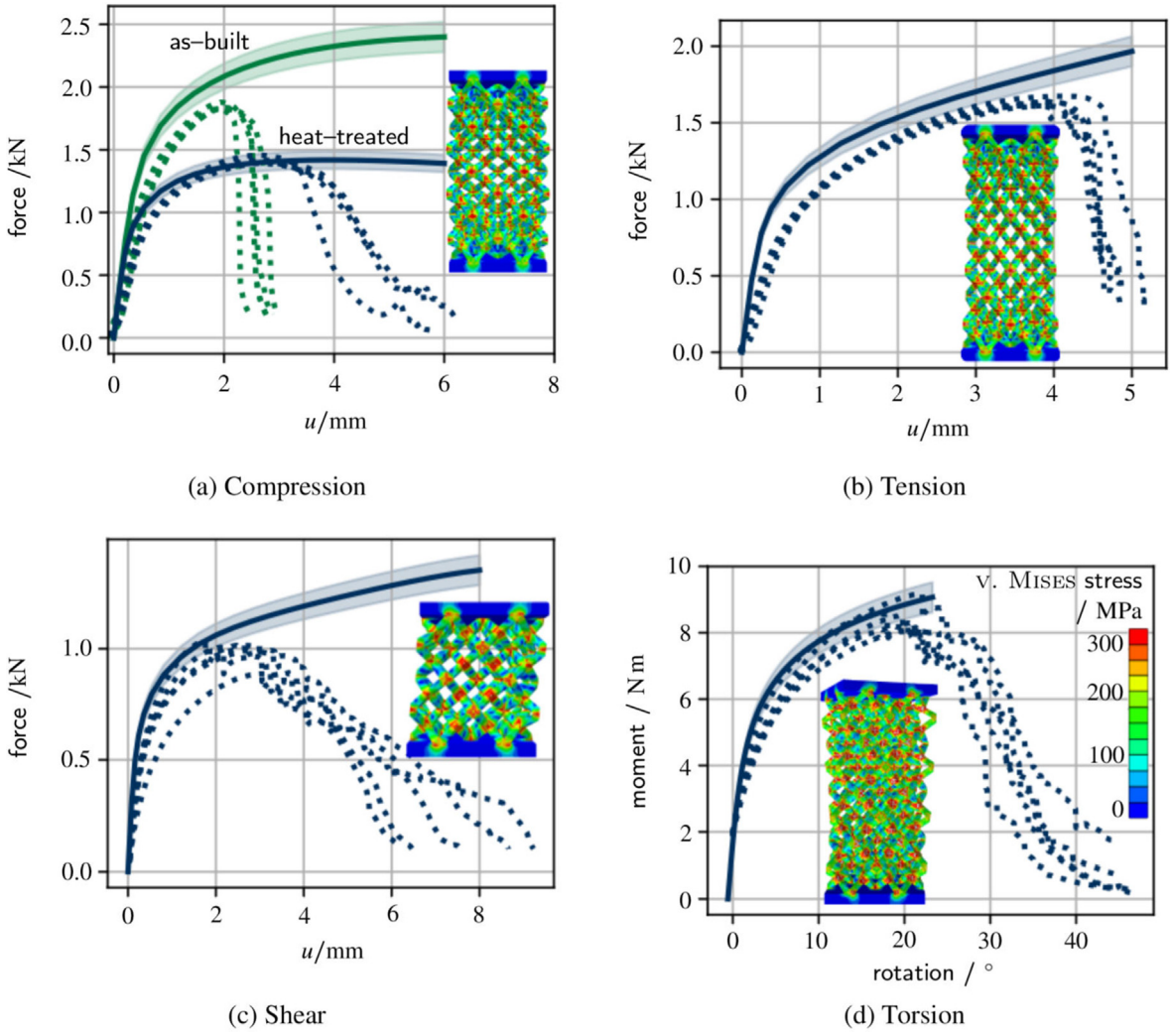

Fig. 9. Comparison of experiments with their virtual equivalents. Dotted lines present the experimental results and the solid lines in the corresponding colour are the virtual experiments belonging to this test setup with a shaded confidence interval of 5%. Green lines refer to as-built lattice specimens and dark blue lines represent lattice specimens which underwent heat treatment after manufacturing. The contour plots show the von Mises stress on the deformed as-designed structure at the point where the maximum force in the corresponding experiment is reached. The legend in (d) refers to all four contour plots. The material model in the contour plots is parametrised with the heat-treated material.

depicted confidence interval of 5% to emphasize the robustness of the presented results. Force–displacement curves of models with twice more refined meshes should all be represented by this confidence interval. Evaluating the experimental results of the compression tests in Fig. 9a, the observed difference between as-built and heat-treated bulk material specimens in subsection 3.2 translates to compression tests on lattice structures. The corresponding numerical results display the same tendency while

a bigger overestimation of the as-built compression tests in comparison to the heat-treated ones is observed. The corresponding contour plots in Fig. 9 show, that maximum stress occurs in the nodal area for all four load setups.

When interpreting the numerical results of this study, the transferability of material parameters acquired from experiments on bulk specimens to lattice structure specimens needs to be discussed. The microstructure of the bulk and lattice specimens is comparable, as discussed in subsection 3.1, and a similar local mechanical behaviour is therefore expected. Size effects and local deviations of the grain size might influence the mechanical behaviour as well. Dong et al. studied size effects on as-built additively manufactured AlSi10Mg and concluded the material parameters to reach the level of cast AlSi10Mg as soon as the struts have a diameter of at least 4 mm [23]. Since the tested bulk parts in this study have a manufactured diameter of 8 mm the characterisation of the bulk material should yield results close to the cast state of that alloy. The struts of the RDC lattice structures have a diameter of 1.4 mm. As DONG ET AL. discovered, the YOUNG moduli of as-built samples decrease by 30% and the ultimate tensile stress decreases by 23% when reducing the diameter of the additively manufactured struts from 5 mm to 1 mm [23]. This reduction in effective stiffness is not inherent to the material model described in Section 3.2 which might partly explain the overestimation of the structural behaviour in Fig. 9. DUMAS ET AL. identified a deviation of 40% when comparing experimental effective stiffness to the effective stiffness of numerical simulations for lattice structures with a structural density of 20%. The effective stiffness increases with decreasing structural density [28]. The lattice structures in this study have an as-designed structural density of 12.6% and an as-manufactured structural density of 14.8%. This difference might explain the overestimation of structural stiffness in all setups.

After the experiments reach their maximum load, the specimens start to break as visualised in the drop of the force–displacement curves. A material model including damage and failure would be needed to numerically predict this effect. The current model only describes the isotropic elastic–plastic behaviour of the material. The rather bad prediction of the compression experiment for as-built lattice specimen might be due to residual stresses in the as-built test specimens which are not taken into account by the model.

The macroscopic geometrical characterisation of manufactured lattice structures via CT and microscopy allows an evaluation of the part quality and conclusions for the differences between the experiments and the as-designed numerical model.

Fig. 10 shows two kinds of imperfections: pores and additional material clinging to the surface. Focusing on porosity first, the visualisation on the top of Fig. 10 qualitatively compares the identified pores of the CT-scan of a node with adjoint struts with a microscopic picture of a cut node. Pores within the lattice structure which were identified by the CT scan and consist of at least eight voxels, as highlighted in the top middle of Fig. 10, have a volume fraction of 1.02%. As shown in subsection 3.2, the bulk specimens have an average volume fraction of pores of 0.085% which is an order of magnitude smaller than the pores in the lattice specimens. Table 5 compares the porosities in the bulk material and the lattice structure with the findings of DONG ET AL. [23]. DONG ET AL. observed a decrease in porosity from 1.87% to 0.1% when investigating struts with a diameter of 1 mm to 5 mm [23]. This tendency agrees with the identified pores in this study. The evaluated size effect in the study of DONG ET AL. is not conclusively linked to the volume fraction of pores within the specimens. SOMBATMAI ET AL. [29] use a titanium instead of an aluminium alloy in their study and consistently observe porosities less than 1% for varying strut sizes from 0.3 mm to 2 mm. Numerical simulations in their study show, that the existing porosity does not influence on the elastic–plastic behaviour of the material in quasi-static test conditions. Therefore, it is concluded that even if the volume fraction of identified pores increases by an order of magnitude when going from material to lattice specimen, the effect of the increased porosity in quasi-static experimental setups with an elastic–plastic material model will be negligible.

In addition to pores as internal imperfections, additional material adheres to the surface of the manufactured lattice structures, as shown in the lower part of Fig. 10. A microscopic image of the very rough surface is qualitatively compared to the registrated structure which identifies the distance of the as-manufactured lattice from the as-designed geometry. Especially the downskin side – the surface facing the building platform during manufacturing – differs greatly from the as-designed structure. Deviations of up to 1 mm are reached. The overall structural density of the as-manufactured lattice structure is calculated to be 14.8%. While the oversizing of struts, which is indicated by the increased as-manufactured structural density, might increase the performance of the structure, LIU ET AL. identified a reduction of effective stiffness by 38% and 15.3% and compressive strength by 34.5% and 14.3% when taking strut deviations for regular octet and rhombicuboctahedral lattice structures into account [27]. Although the struts in this study are less slender than the ones investigated by LIU ET AL. and the observed sensitivity decreases with the decreasing slenderness, some effect from these imperfections on the mechanical behaviour is to be expected as well. These relationships will be more deeply investigated in the near future and are out of scope for the described study.

4. Conclusion

The study presents systematic experiments, characterisation and modelling of additively manufactured bulk material and lattice structures. Test specimens for tension tests on the bulk material and for compression, tension, shear and torsion tests on the lattice structures were manufactured and mechanically and microstructurally characterised – both for as-built and heat-treated specimens. The results of the bulk material tests have been successfully used to parametrise an elastic–plastic material model. Imperfections within the bulk material were characterised and inherently included in the material model. With this material model virtual experiments on as-designed lattice structures in compression, tension, shear and torsion were performed and compared to their experimental equivalents. Differences between virtual tests and experiments were discussed with respect to imperfections and findings from other studies.

The main findings of this study are:

- The Si network decomposes after heat treatment and is therefore a key issue for a reduced tensile strength and increased elongation. This applies to rather complex structures (lattices) as well as bulk samples and is therefore responsible for reduced tensile strength and increased elongation in the heat-treated samples compared to as-built specimens.
- A detailed microstructural study revealed no obvious differences (phase formation, grain sizes) between bulk and lattice specimens in the heat-treated condition. A similar local mechanical behaviour was therefore expected and allowed the transfer of material parameters identified on the bulk material to lattice structures.
- An elastic–plastic material model captures the mechanical behaviour of bulk material specimens up to 2.5% and 15% true strain for as-built and heat-treated specimens respectively.

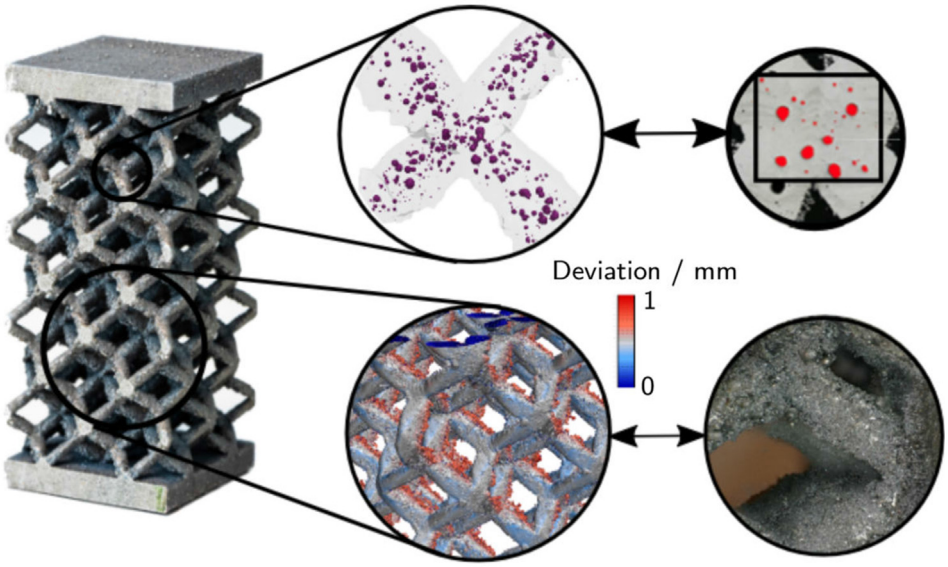

Fig. 10. Imperfections in the manufactured lattice structure (left): Identified pores from CT scan (top middle) and from optical microscopy (top right, the same sample as analysed in Fig. 5 (c)) and additional material visualised through the distance of the CT's surface to the surface of the as-designed geometry (bottom middle) and optical microscopy. (bottom right).

Table 5
Identified pores in this study compared to literature.

Source	Material	Specimen	Strut diameter/ mm	Volume fraction of identified pores/ %
This work	AlSi10Mg	Bulk material	8 (4 post – treated)	0.085
		Lattice structure	1.4 (as-designed)	1.02
Dong [23]	AlSi10Mg	tension test specimens	1	1.87
			3	0.57
			5	0.10

- Mesh settings with quadratic tetrahedral elements and an element size of at least 5.5 elements per strut-diameter yield satisfying results in terms of a balanced cost-benefit ratio when evaluating the work up to maximum force for the structural behaviour for as-designed lattice structures with a RDC unit cell and no additional radii at its sharp corners.
- The presented model is able to predict the overall behaviour of lattice structure specimens with their as-designed geometry in varying test setups, including compression, tension, shear and torsion tests.
- The imperfections in the bulk as well as lattice specimens qualitatively and quantitatively fit to reported values in the literature. Effects from these imperfections on the mechanical performance of the structures, as they are studied in the literature [27,31], also confirmed our findings regarding the difference between experiments and simulations in this study.

The presented RDC lattice structure has thicker struts than lattices from comparable studies [27,31]. Since the tendency of the evaluation of imperfections with the strut sizes from literature agrees with the presented results, a conclusion might be drawn that for the investigated alloy there is a minimum strut thickness for additively manufactured lattice structures from where process-induced imperfections have negligible influence on the mechanical performance of the structure. Especially pores are known to not affect the quasi-static test setups [29] but play an important role when looking into the fatigue behaviour of additively manufactured lattice structures [2]. This also suggests, that the presented model in this study will not yield as good results when applied to other lattice geometries with more slender struts. Even though imperfections are not included in the presented numerical model, the models containing more than one million elements are already very large. If the model is able to predict the mechanical behaviour of a complex part, depends on the size of the model and the included lattice structure as well as the available resources. With the resources available for this study, small parts or parts with smaller confined areas of lattice structures should be possible to investigate.

Further research will be aimed to investigate sensitivities of the performance of lattice structure specimens with respect to macroscopic imperfections as well as damage initiation and damage behaviour. Also the fatigue behaviour for such structures is of interest and will require further experiments. One of the next steps should be to transfer the obtained findings to a material-dependent database in which the strut diameter and further requirements like inclination angle, surface quality and/or uniformity are assigned to optimised parameter sets. This optimisation would offer new possibilities for the design and additive manufacturing of complex lightweight components for possible future applications (e.g. load-bearing brackets).

Funding

This research did not receive any specific grant from funding agencies in the public, commercial, or not-for-profit sectors.

CRediT authorship contribution statement

Ulrike Gebhardt: Conceptualization, Methodology, Investigation, Modelling, Visualisation, Writing and Editing Original draft.

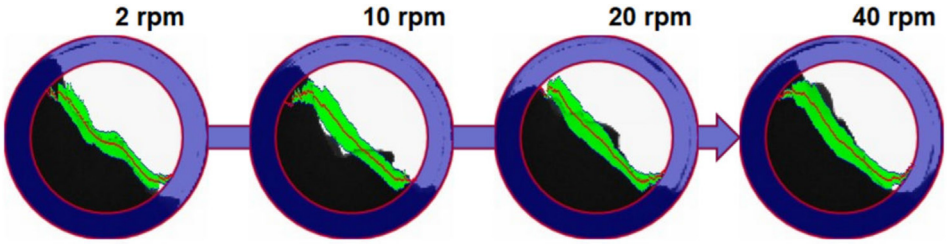

Fig. 11. 2D images of the flow of a powder sample during testing in a GranuDrum device. Only the pictures for the forward sequence (backward sequence: decreasing rotation speed) are shown. The images reveal the average dynamic angle of response (plotted in red) as a function of the rotating speed: 2 rpm = 38.1°, 10 rpm = 46.5°, 20 rpm = 45.8°, 40 rpm = 47.2°. The green area, surrounding the dynamic angle of response line, implies the dynamic cohesive index which is measured from the interface fluctuation and increases with increasing rotation speed (2 rpm: cohesion index = 17.1, 20 rpm: cohesion index = 20.4).

Tobias Gustmann: Conceptualization, Methodology, Investigation, Visualisation, Writing and Editing Original draft, Proofreading. **Lars Giebeler:** Methodology, Investigation, Writing and Editing – Original draft. **Franz Hirsch:** Methodology, Visualisation – Original draft, Proofreading. **Julia Kristin Hufenbach:** Conceptualization, Writing and Editing – Original draft, Proofreading. **Markus Kästner:** Conceptualization, Methodology – Original draft, Proofreading.

Data availability

The raw/processed data required to reproduce these findings cannot be shared at this time as the data also forms part of an ongoing study.

Declaration of Competing Interest

The authors declare that they have no known competing financial interests or personal relationships that could have appeared to influence the work reported in this paper.

Acknowledgements

The authors would like to thank S. Blobel and S. Holtzhausen as well as J. Sander, P. Wang, S. Pilz, N. Geißler, R. Keller, H. Bußkamp and A. Voß for their technical support and insight. M. Berner, R. Gärtner and C. Läßig with the Leichtbau-Zentrum Sachsen GmbH are gratefully acknowledged for their initial work and the mechanical characterisation. Furthermore, the authors very much appreciate the support by Dr. Uta Kühn. The research shown did not receive any specific grant from funding agencies in the public or commercial sector. The computations were performed on a PC-Cluster at the Center for Information Services and High Performance Computing (ZIH) at TU Dresden. The authors thank the ZIH for generous allocations of computer time.

Appendix A. Additional information on powder characterisation

Fig. 11 shows the results of the dynamic measurements with a rotating drum.

References

[1] J. Hufenbach, J. Sander, F. Kochta, S. Pilz, A. Voss, U. Kühn, et al., Effect of selective laser melting on microstructure, mechanical, and corrosion properties of biodegradable FeMnCS for implant applications, Adv. Eng. Mater. 22 (10) (2020) 2000182, https://doi.org/10.1002/adem.202000182. URL: https://onlinelibrary.wiley.com/doi/10.1002/adem.202000182.

[2] T. Maconachie, M. Leary, B. Lozanovski, X. Zhang, M. Qian, O. Faruque, et al., SLM lattice structures: Properties, performance, applications and challenges, Materials & Design 183 (2019) 108137, https://doi.org/10.1016/j.matdes.2019.108137. URL: https://linkinghub.elsevier.com/retrieve/pii/S0264127519305751.

[3] A. du Plessis, S.M.J. Razavi, M. Benedetti, S. Murchio, M. Leary, M. Watson, et al., Properties and applications of additively manufactured metallic cellular materials: A review, Prog. Mater Sci. 125 (2022) 100918, https://doi.org/10.1016/j.pmatsci.2021.100918. URL: https://www.sciencedirect.com/science/article/pii/S0079642521001420.

[4] Z. Alomar, F. Concli, A review of the selective laser melting lattice structures and their numerical models, Adv. Eng. Mater. 22 (12) (2020) 2000611, https://doi.org/10.1002/adem.202000611. URL: https://onlinelibrary.wiley.com/doi/10.1002/adem.202000611.

[5] X. Li, X. Wang, M. Saunders, A. Suvorova, L. Zhang, Y. Liu, et al., A selective laser melting and solution heat treatment refined Al–12Si alloy with a controllable ultrafine eutectic microstructure and 25% tensile ductility, Acta Mater. 95 (2015) 74–82, https://doi.org/10.1016/j.actamat.2015.05.017. URL: https://linkinghub.elsevier.com/retrieve/pii/S1359645415003389.

[6] K. Prashanth, S. Scudino, J. Eckert, Defining the tensile properties of Al-12Si parts produced by selective laser melting, Acta Mater. 126 (2017) 25–35, https://doi.org/10.1016/j.actamat.2016.12.044. URL: https://linkinghub.elsevier.com/retrieve/pii/S135964541630982X.

[7] K. Prashanth, S. Scudino, H. Klauss, K. Surreddi, L. Löber, Z. Wang, et al., Microstructure and mechanical properties of Al–12Si produced by selective laser melting: Effect of heat treatment, Materials Science and Engineering: A 590 (2014) 153–160, https://doi.org/10.1016/j.msea.2013.10.023. URL: https://linkinghub.elsevier.com/retrieve/pii/S0921509313011180.

[8] K. Prashanth, B. Debalina, Z. Wang, P. Gostin, A. Gebert, M. Calin, et al., Tribological and corrosion properties of Al–12Si produced by selective laser melting, J. Mater. Res. 29 (17) (2014) 2044–2054, https://doi.org/10.1557/jmr.2014.133. URL: http://link.springer.com/10.1557/jmr.2014.133.

[9] N. Read, W. Wang, K. Essa, M.M. Attallah, Selective laser melting of AlSi10Mg alloy: Process optimisation and mechanical properties development, Materials & Design (1980–2015) 65 (2015) 417–424, https://doi.org/10.1016/j.matdes.2014.09.044. URL https://linkinghub.elsevier.com/retrieve/pii/S0261306914007468.

[10] J. Suryawanshi, K. Prashanth, S. Scudino, J. Eckert, O. Prakash, U. Ramamurty, Simultaneous enhancements of strength and toughness in an Al-12Si alloy synthesized using selective laser melting, Acta Mater. 115 (2016) 285–294, https://doi.org/10.1016/j.actamat.2016.06.009. URL: https://linkinghub.elsevier.com/retrieve/pii/S1359645416304281.

[11] L. Thijs, K. Kempen, J.P. Kruth, J. Van Humbeeck, Fine-structured aluminium products with controllable texture by selective laser melting of pre-alloyed AlSi10Mg powder, Acta Mater. 61 (5) (2013) 1809–1819, https://doi.org/10.1016/j.actamat.2012.11.052. URL: https://linkinghub.elsevier.com/retrieve/pii/S1359645412008592.

[12] F. Trevisan, F. Calignano, M. Lorusso, J. Pakkanen, A. Aversa, E. Ambrosio, et al., On the selective laser melting (SLM) of the AlSi10Mg alloy: Process, microstructure, and mechanical properties, Materials 10 (1) (2017) 76, https://doi.org/10.3390/ma10010076. URL: http://www.mdpi.com/1996-1944/10/1/76.

[13] P. Wei, Z. Wei, Z. Chen, J. Du, Y. He, J. Li, et al., The AlSi10Mg samples produced by selective laser melting: single track, densification, microstructure and mechanical behavior, Appl. Surf. Sci. 408 (2017) 38–50, https://doi.org/10.1016/j.apsusc.2017.02.215. URL: https://linkinghub.elsevier.com/retrieve/pii/S0169433217305883.

[14] A. Kempf, K. Hilgenberg, Influence of sub-cell structure on the mechanical properties of AlSi10Mg manufactured by laser powder bed fusion, Materials Science and Engineering: A 776 (2020) 138976, https://doi.org/10.1016/j.msea.2020.138976. URL: https://linkinghub.elsevier.com/retrieve/pii/S0921509320300654.

[15] K. Riener, N. Albrecht, S. Ziegelmeier, R. Ramakrishnan, L. Haferkamp, A.B. Spierings, et al., Influence of particle size distribution and morphology on the properties of the powder feedstock as well as of AlSi10Mg parts produced by laser powder bed fusion (LPBF), Additive Manufacturing 34 (2020) 101286, https://doi.org/10.1016/j.addma.2020.101286. URL: https://linkinghub.elsevier.com/retrieve/pii/S2214860420306588.

[16] K. Riener, S. Oswald, M. Winkler, G.J. Leichtfried, Influence of storage conditions and reconditioning of AlSi10Mg powder on the quality of parts

produced by laser powder bed fusion (LPBF), Additive Manufacturing 39 (2021) 101896, https://doi.org/10.1016/j.addma.2021.101896. URL: https://linkinghub.elsevier.com/retrieve/pii/S2214860421000610.
[17] C. Weingarten, D. Buchbinder, N. Pirch, W. Meiners, K. Wissenbach, R. Poprawe, Formation and reduction of hydrogen porosity during selective laser melting of AlSi10Mg, J. Mater. Process. Technol. 221 (2015) 112–120, https://doi.org/10.1016/j.jmatprotec.2015.02.013. URL: https://linkinghub.elsevier.com/retrieve/pii/S0924013615000564.
[18] J. Oliveira, A. LaLonde, J. Ma, Processing parameters in laser powder bed fusion metal additive manufacturing, Materials & Design 193 (2020) 108762, https://doi.org/10.1016/j.matdes.2020.108762. URL: https://linkinghub.elsevier.com/retrieve/pii/S0264127520302963.
[19] J.G. Santos Macías, T. Douillard, L. Zhao, E. Maire, G. Pyka, A. Simar, Influence on microstructure, strength and ductility of build platform temperature during laser powder bed fusion of AlSi10Mg, Acta Mater. 201 (2020) 231–243, https://doi.org/10.1016/j.actamat.2020.10.001. URL: https://linkinghub.elsevier.com/retrieve/pii/S1359645420307904.
[20] A. Aversa, G. Marchese, A. Saboori, E. Bassini, D. Manfredi, S. Biamino, et al., New aluminum alloys specifically designed for laser powder bed fusion: A review, Materials 12 (7) (2019) 1007, https://doi.org/10.3390/ma12071007. URL: https://www.mdpi.com/1996-1944/12/7/1007.
[21] A. Mauduit, S. Pillot, H. Gransac, Study of the suitability of aluminum alloys for additive manufacturing by laser powder bed fusion, Sci Bull 79 (4) (2017) 219–238. URL https://cetimcentrevaldeloire.fr/wp-content/uploads/2018/03/Study-of-the-suitability-of-Al-alloys-for-AM-by-laser-powder-bed-fusion.pdf.
[22] P. Van Cauwenbergh, V. Samaee, L. Thijs, J. Nejezchlebová, P. Sedlák, A. Ivekovic, et al., Unravelling the multi-scale structure–property relationship of laser powder bed fusion processed and heat-treated AlSi10Mg, Scientific Reports 11 (1) (2021) 6423, https://doi.org/10.1038/s41598-021-85047-2. URL: https://www.nature.com/articles/s41598-021-85047-2.
[23] Z. Dong, X. Zhang, W. Shi, H. Zhou, H. Lei, J. Liang, Study of size effect on microstructure and mechanical properties of AlSi10Mg samples made by selective laser melting, Materials 11 (12) (2018) 2463, https://doi.org/10.3390/ma11122463. URL: https://www.mdpi.com/1996-1944/11/12/2463.
[24] R. Baitimerov, P. Lykov, D. Zherebtsov, L. Radionova, A. Shultc, K. Prashanth, Influence of powder characteristics on processability of AlSi12 alloy fabricated by selective laser melting, Materials 11 (5) (2018) 742, https://doi.org/10.3390/ma11050742. URL: http://www.mdpi.com/1996-1944/11/5/742.
[25] N.T. Aboulkhair, I. Maskery, C. Tuck, I. Ashcroft, N.M. Everitt, The microstructure and mechanical properties of selectively laser melted AlSi10Mg: The effect of a conventional T6-like heat treatment, Materials Science and Engineering: A 667 (2016) 139–146, https://doi.org/10.1016/j.msea.2016.04.092. URL: https://linkinghub.elsevier.com/retrieve/pii/S0921509316304890.
[26] N. Takata, H. Kodaira, K. Sekizawa, A. Suzuki, M. Kobashi, Change in microstructure of selectively laser melted AlSi10Mg alloy with heat treatments, Materials Science and Engineering: A 704 (2017) 218–228, https://doi.org/10.1016/j.msea.2017.08.029. URL: https://linkinghub.elsevier.com/retrieve/pii/S0921509317310353.
[27] L. Liu, P. Kamm, F. García-Moreno, J. Banhart, D. Pasini, Elastic and failure response of imperfect three-dimensional metallic lattices: the role of geometric defects induced by selective laser melting, J. Mech. Phys. Solids 107 (2017) 160–184, https://doi.org/10.1016/j.jmps.2017.07.003. URL: http://www.sciencedirect.com/science/article/pii/S0022509616307608.
[28] M. Dumas, P. Terriault, V. Brailovski, Modelling and characterization of a porosity graded lattice structure for additively manufactured biomaterials, Materials & Design 121 (2017) 383–392, https://doi.org/10.1016/j.matdes.2017.02.021. URL: https://linkinghub.elsevier.com/retrieve/pii/S0264127517301491.
[29] A. Sombatmai, V. Uthaisangsuk, S. Wongwises, P. Promoppatum, Multiscale investigation of the influence of geometrical imperfections, porosity, and size-dependent features on mechanical behavior of additively manufactured Ti-6Al-4V lattice struts, Materials & Design 209 (2021) 109985, https://doi.org/10.1016/j.matdes.2021.109985. URL: https://www.sciencedirect.com/science/article/pii/S0264127521005396.
[30] X. Wang, R. Qin, B. Chen, Laser-based additively manufactured bio-inspired crashworthy structure: Energy absorption and collapse behaviour under static and dynamic loadings, Materials & Design 211 (2021) 110128, https://doi.org/10.1016/j.actamat.2018.08.030. URL: https://www.sciencedirect.com/science/article/pii/S0264127521006833.
[31] Y. Amani, S. Dancette, P. Delroisse, A. Simar, E. Maire, Compression behavior of lattice structures produced by selective laser melting: X-ray tomography based experimental and finite element approaches, Acta Mater. 159 (2018) 395–407, https://doi.org/10.1016/j.actamat.2018.08.030. URL: https://linkinghub.elsevier.com/retrieve/pii/S1359645418306670.
[32] M. Costas, D. Morin, M. de Lucio, M. Langseth, Testing and simulation of additively manufactured AlSi10Mg components under quasi-static loading, Eur. J. Mech. A. Solids 81 (2020) 103966, https://doi.org/10.1016/j.euromechsol.2020.103966. URL: https://linkinghub.elsevier.com/retrieve/pii/S0997753819306758.
[33] F. Nalli, L. Cortese, F. Concli, Ductile damage assessment of Ti6Al4V, 17–4PH and AlSi10Mg for additive manufacturing, Eng. Fract. Mech. 241 (2021) 107395, https://doi.org/10.1016/j.engfracmech.2020.107395. URL: https://www.sciencedirect.com/science/article/pii/S0013794420309747.
[34] S. Romano, A. Brückner-Foit, A. Brandão, J. Gumpinger, T. Ghidini, S. Beretta, Fatigue properties of AlSi10Mg obtained by additive manufacturing: Defect-based modelling and prediction of fatigue strength, Eng. Fract. Mech. 187 (2018) 165–189, https://doi.org/10.1016/j.engfracmech.2017.11.002. URL: https://linkinghub.elsevier.com/retrieve/pii/S0013794417310068.
[35] A. Zargarian, M. Esfahanian, J. Kadkhodapour, S. Ziaei-Rad, D. Zamani, On the fatigue behavior of additive manufactured lattice structures, Theoret. Appl. Fract. Mech. 100 (2019) 225–232, https://doi.org/10.1016/j.tafmec.2019.01.012. URL: https://linkinghub.elsevier.com/retrieve/pii/S0167844218302234.
[36] K.G. Prashanth, L. Löber, H.J. Klauss, U. Kühn, J. Eckert, Characterization of 316L steel cellular dodecahedron structures produced by selective laser melting, Technologies 4 (4) (2016) 34, https://doi.org/10.3390/technologies4040034. URL: https://www.mdpi.com/2227-7080/4/4/34.
[37] F.J.Q. Gonzalez, N. Nuno, Finite element modeling of manufacturing irregularities of porous materials, Biomaterials and Biomechanics in Bioengineering 3 (1) (2016) 1–14, https://doi.org/10.12989/BME.2016.3.1.001. URL: https://doi.org/10.12989/BME.2016.3.1.001.
[38] Mantovani, S., Giacalone, M., Merulla, A., Bassoli, E., Defanti, S. Effective mechanical properties of AlSi7Mg additively manufactured cubic lattice structures. 3D Printing and Additive Manufacturing 2021;0:3dp.2021.0176. doi:10.1089/3dp.2021.0176. URL: https://www.liebertpub.com/doi/10.1089/3dp.2021.0176.
[39] K.M. Park, K.S. Min, Y.S. Roh, Design optimization of lattice structures under compression: Study of unit cell types and cell arrangements, Materials 15 (1) (2021) 97, https://doi.org/10.3390/ma15010097. URL: https://www.mdpi.com/1996-1944/15/1/97.
[40] X. Wang, L. Zhu, L. Sun, N. Li, Optimization of graded filleted lattice structures subject to yield and buckling constraints, Materials & Design 206 (2021) 109746, https://doi.org/10.1016/j.matdes.2021.109746. URL: https://linkinghub.elsevier.com/retrieve/pii/S0264127521002999.
[41] T. Gustmann, F. Gutmann, F. Wenz, P. Koch, R. Stelzer, W.G. Drossel, et al., Properties of a superelastic NiTi shape memory alloy using laser powder bed fusion and adaptive scanning strategies, Progress in Additive Manufacturing 5 (1) (2020) 11–18, https://doi.org/10.1007/s40964-020-00118-6. URL: http://link.springer.com/10.1007/s40964-020-00118-6.
[42] P. Delroisse, P.J. Jacques, E. Maire, O. Rigo, A. Simar, Effect of strut orientation on the microstructure heterogeneities in AlSi10Mg lattices processed by selective laser melting, Scripta Mater. 141 (2017) 32–35, https://doi.org/10.1016/j.scriptamat.2017.07.020. URL: https://linkinghub.elsevier.com/retrieve/pii/S1359646217304256.
[43] H. Lei, C. Li, J. Meng, H. Zhou, Y. Liu, X. Zhang, et al., Evaluation of compressive properties of SLM-fabricated multi-layer lattice structures by experimental test and μ-CT-based finite element analysis, Materials & Design 169 (2019) 107685, https://doi.org/10.1016/j.matdes.2019.107685. URL: https://linkinghub.elsevier.com/retrieve/pii/S0264127519301224.
[44] B. Lozanovski, M. Leary, P. Tran, D. Shidid, M. Qian, P. Choong, et al., Computational modelling of strut defects in SLM manufactured lattice structures, Materials & Design 171 (2019) 107671, https://doi.org/10.1016/j.matdes.2019.107671. URL: https://linkinghub.elsevier.com/retrieve/pii/S026412751930108X.
[45] M.R.K. Ravari, S.N. Esfahani, M.T. Andani, M. Kadkhodaei, A. Ghaei, H. Karaca, et al., On the effects of geometry, defects, and material asymmetry on the mechanical response of shape memory alloy cellular lattice structures, Smart Mater. Struct. 25 (2) (2016) 025008, https://doi.org/10.1088/0964-1726/25/2/025008. URL: http://stacks.iop.org/0964-1726/25/i=2/a=025008?key=crossref.4f4ae5ff46699b322954e6fdfaa87934.
[46] S. Siddique, M. Imran, M. Rauer, M. Kaloudis, E. Wycisk, C. Emmelmann, et al., Computed tomography for characterization of fatigue performance of selective laser melted parts, Materials & Design 83 (2015) 661–669, https://doi.org/10.1016/j.matdes.2015.06.063. URL: http://linkinghub.elsevier.com/retrieve/pii/S026412751500413X.
[47] M. Carraturo, G. Alaimo, S. Marconi, E. Negrello, E. Sgambitterra, C. Maletta, et al., Experimental and numerical evaluation of mechanical properties of 3D-printed stainless steel 316L lattice structures, J. Mater. Eng. Perform. (2021), https://doi.org/10.1007/s11665-021-05737-w. URL: https://link.springer.com/10.1007/s11665-021-05737-w.
[48] L. Geng, B. Zhang, Y. Lian, R. Gao, D. Fang, An image-based multi-level hp fcm for predicting elastoplastic behavior of imperfect lattice structure by slm, Comput. Mech. (2022) 1–18, https://doi.org/10.1007/s00466-022-02158-x. URL: https://doi.org/10.1007/s00466-022-02158-x.
[49] F. Brenne, T. Niendorf, Load distribution and damage evolution in bending and stretch dominated Ti-6Al-4V cellular structures processed by selective laser melting, Int. J. Fatigue 121 (2019) 219–228, https://doi.org/10.1016/j.ijfatigue.2018.12.017. URL: https://www.sciencedirect.com/science/article/pii/S0142112318307345.
[50] R. Goodall, E. Hernandez-Nava, S.N.M. Jenkins, L. Sinclair, E. Tyrwhitt-Jones, M. A. Khodadadi, et al., The effects of defects and damage in the mechanical behavior of Ti6Al4V lattices, Frontiers in Materials 6 (2019) 117, https://doi.org/10.3389/fmats.2019.00117. URL: https://www.frontiersin.org/article/10.3389/fmats.2019.00117/full.
[51] H. Mehboob, F. Tarlochan, A. Mehboob, S.H. Chang, Finite element modelling and characterization of 3D cellular microstructures for the design of a cementless biomimetic porous hip stem, Materials & Design 149 (2018) 101–112, https://doi.org/10.1016/j.matdes.2018.04.002. URL: https://linkinghub.elsevier.com/retrieve/pii/S0264127518302648.
[52] E.G. Brodie, T. Wegener, J. Richter, A. Medvedev, T. Niendorf, A. Molotnikov, A mechanical comparison of alpha and beta phase biomedical tita lattice

structures, Materials & Design 212 (2021) 110220, https://doi.org/10.1016/j.matdes.2021.110220. URL: https://www.sciencedirect.com/science/article/pii/S0264127521007759.
[53] F. Di Caprio, S. Franchitti, R. Borrelli, C. Bellini, V. Di Cocco, L. Sorrentino, Ti-6Al-4V octet-truss lattice structures under bending load conditions: Numerical and experimental results, Metals 12 (3) (2022) 410, https://doi.org/10.3390/met12030410. URL: https://www.mdpi.com/2075-4701/12/3/410.
[54] SLM Solutions,. Material data sheet. 2021. URL: https://www.slm-solutions.com/fileadmin/Content/Powder/MDS/MDS_Al-Alloy_AlSi10Mg_0520_EN.pdf.
[55] S. Vock, B. Klöden, A. Kirchner, T. Weißgärber, B. Kieback, Powders for powder bed fusion: a review, Progress in Additive Manufacturing 4 (4) (2019) 383–397, https://doi.org/10.1007/s40964-019-00078-6. URL: http://link.springer.com/10.1007/s40964-019-00078-6.
[56] G. Del Guercio, M. Galati, A. Saboori, Innovative approach to evaluate the mechanical performance of Ti–6Al–4V lattice structures produced by electron beam melting process, Met. Mater. Int. 27 (1) (2021) 55–67, https://doi.org/10.1007/s12540-020-00745-2. URL: http://link.springer.com/10.1007/s12540-020-00745-2.
[57] H.M. Rietveld, A profile refinement method for nuclear and magnetic structures, J. Appl. Crystallogr. 2 (2) (1969) 65–71, https://doi.org/10.1107/S0021889869006558. URL: https://onlinelibrary.wiley.com/doi/10.1107/S0021889869006558.
[58] T. Roisnel, J. Rodríquez-Carvajal, WinPLOTR: a windows tool for powder diffraction pattern analysis, Mater. Sci. Forum 378 (2001) 118–123, https://doi.org/10.4028/www.scientific.net/MSF.378-381.118. URL: https://www.scientific.net/MSF.378-381.118.
[59] Debye, P., Scherrer, P. Interferenzen an regellos orientierten teilchen im Röntgenlicht. I. Nachrichten von der Gesellschaft der Wissenschaften zu Göttingen, Mathematisch-Physikalische Klasse 1916;1916:1–15. URL: https://eudml.org/doc/58947.
[60] A.W. Hull, A new method of x-ray crystal analysis, Phys. Rev. 10 (6) (1917) 661, https://doi.org/10.1103/PhysRev.10.661. URL: https://link.aps.org/doi/10.1103/PhysRev.10.661.
[61] Owen, E., Preston, G. The atomic structure of two intermetallic compounds. Proceedings of the Physical Society of London (1874–1925) 1923;36(1):341. URL: https://iopscience.iop.org/article/10.1088/1478-7814/36/1/339. doi:10.1088/1478-7814/36/1/339.
[62] Dassault Systemes, Abaqus Manual. 2020. URL: https://help.3ds.com/.
[63] U. Gebhardt, R. Gärtner, M. Berner, S. Holtzhausen, J.K. Hufenbach, U. Kühn, et al., Virtual testing of additively manufactured grid structures, Proceeding in Applied Mathematics and Mechanics 19 (1) (2019), https://doi.org/10.1002/pamm.201900330. URL https://onlinelibrary.wiley.com/doi/abs/10.1002/pamm.201900330.
[64] H.W. Swift, Plastic instability under plane stress, J. Mech. Phys. Solids 1 (1) (1952) 1–18, https://doi.org/10.1016/0022-5096(52)90002-1. URL: http://www.sciencedirect.com/science/article/pii/0022509652900021.
[65] R.W. Swindeman, Representation of the High-Temperature Tensile Behavior of Reannealed Type 304 Stainless Steel by the Voce Equation, J. Eng. Mater. Technol. 97 (2) (1975) 98–106, https://doi.org/10.1115/1.3443284.
[66] A. Hadadzadeh, B.S. Amirkhiz, M. Mohammadi, Contribution of Mg_2Si precipitates to the strength of direct metal laser sintered AlSi10Mg, Materials Science and Engineering: A 739 (2019) 295–300, https://doi.org/10.1016/j.msea.2018.10.055. URL: https://linkinghub.elsevier.com/retrieve/pii/S0921509318314266.
[67] A.H. Maamoun, M. Elbestawi, G.K. Dosbaeva, S.C. Veldhuis, Thermal post-processing of AlSi10Mg parts produced by selective laser melting using recycled powder, Additive Manufacturing 21 (2018) 234–247, https://doi.org/10.1016/j.addma.2018.03.014. URL: https://linkinghub.elsevier.com/retrieve/pii/S2214860418300617.
[68] S. Pauly, P. Wang, U. Kühn, K. Kosiba, Experimental determination of cooling rates in selectively laser-melted eutectic Al-33Cu, Additive Manufacturing 22 (2018) 753–757, https://doi.org/10.1016/j.addma.2018.05.034. URL: https://linkinghub.elsevier.com/retrieve/pii/S2214860418300733.
[69] E. Sert, L. Hitzler, S. Hafenstein, M. Merkel, E. Werner, A. Öchsner, Tensile and compressive behaviour of additively manufactured AlSi10Mg samples, Progress in Additive Manufacturing 5 (3) (2020) 305–313, https://doi.org/10.1007/s40964-020-00131-9. URL: http://link.springer.com/10.1007/s40964-020-00131-9.
[70] N.T. Aboulkhair, M. Simonelli, L. Parry, I. Ashcroft, C. Tuck, R. Hague, 3D printing of aluminium alloys: Additive manufacturing of aluminium alloys using selective laser melting, Prog. Mater Sci. 106 (2019) 100578, https://doi.org/10.1016/j.pmatsci.2019.100578. URL: https://linkinghub.elsevier.com/retrieve/pii/S007964251930060X.
[71] J. Liu, P. Wen, Metal vaporization and its influence during laser powder bed fusion process, Materials & Design 215 (2022) 110505, https://doi.org/10.1016/j.matdes.2022.110505. URL: https://www.sciencedirect.com/science/article/pii/S0264127522001265.
[72] C. Tenbrock, T. Kelliger, N. Praetzsch, M. Ronge, L. Jauer, J.H. Schleifenbaum, Effect of laser-plume interaction on part quality in multi-scanner laser powder bed fusion, Additive Manufacturing 38 (2021) 101810, https://doi.org/10.1016/j.addma.2020.101810. URL: https://linkinghub.elsevier.com/retrieve/pii/S2214860420311829.
[73] Fiegl, T., Franke, M., Raza, A., Hryha, E., Körner, C.. Effect of AlSi10Mg0.4 long-term reused powder in PBF-LB/M on the mechanical properties. Materials & Design 2021;212:110176. doi:10.1016/j.matdes.2021.110176. URL: https://www.sciencedirect.com/science/article/pii/S0264127521007310.
[74] J. Fiocchi, A. Tuissi, C.A. Biffi, Heat treatment of aluminium alloys produced by laser powder bed fusion: A review, Materials & Design 204 (2021) 109651, https://doi.org/10.1016/j.matdes.2021.109651. URL: https://www.sciencedirect.com/science/article/pii/S0264127521002045.
[75] E. Sert, E. Schuch, A. Öchsner, L. Hitzler, E. Werner, M. Merkel, Tensile strength performance with determination of the Poisson's ratio of additively manufactured AlSi10Mg samples, Materialwiss. Werkstofftech. 50 (5) (2019) 539–545, https://doi.org/10.1002/mawe.201800233. URL: https://onlinelibrary.wiley.com/doi/abs/10.1002/mawe.201800233.